THE JOURNAL OF PHYSICAL CHEMISTRY C

pubs.acs.org/JPCC Article

Observation of $[V_{Cu}^{1-}In_i^{2+}V_{Cu}^{1-}]$ Defect Triplets in Cu-Deficient $CuInS_2$

Published as part of The Journal of Physical Chemistry virtual special issue "Emily A. Carter Festschrift".

Jessica J. Frick,* Guangming Cheng, Satya Kushwaha, Nan Yao, Sigurd Wagner,* Andrew B. Bocarsly, and Robert J. Cava

Cite This: *J. Phys. Chem. C* 2020, 124, 26415−26427 Read Online

ACCESS | Metrics & More | Article Recommendations | Supporting Information

ABSTRACT: Copper indium disulfide ($CuInS_2$) is a semiconductor with a direct energy band gap of 1.53 eV—an optimal value for highly efficient thin-film solar cells. But it has reached only ∼11% power conversion efficiency, far less than the theoretically achievable value of ∼30%. The cause of this low performance is not understood. A single crystal grown from 1 mol % Cu-deficient melt was studied by using atomic resolution high-angle annular dark-field (HAADF) scanning transmission electron microscopy (STEM) and electron dispersive spectroscopy (EDS). While the bulk crystal is exactly stoichiometric $CuInS_2$, it contains nanometer thick, structurally coherent, Cu-deficient interphases that form along rotational twin boundaries in the {112} plane. Transition zones from the bulk crystal to the interphase are observed, where In is seen to move from its normal site In_{In} in the chalcopyrite structure to a tetrahedral interstitial site In_i, while Cu remains in its normal Cu_{Cu} position. Two In_{In} rows of the bulk crystal merge into one row of In_i, causing excess In_i in the interphase. The concentrations of Cu_{Cu} and In_i reflect a ratio of Cu vacancies, V_{Cu}, to an excess In_i of ∼2. Their relative lattice positions, and the high electrical resistivity of the crystal, suggest that V_{Cu} and excess In_i "precipitate" as self-compensating, electrically neutral, $[V_{Cu}^{1-}In_i^{2+}V_{Cu}^{1-}]$ defect triplets. This is the first atomic-level observation of the ordered defect that has been invoked as the basic structural modifier in chalcopyrite compound homologues. The interphases introduce an optical gap of 1.47 eV. Electron trapping in band tail states, evident from a photoconductivity exponent of 0.54, is the likely cause of an unusually low electron mobility of 0.1 $cm^2\ V^{-1}\ s^{-1}$. The overall result is that making $CuInS_2$ slightly copper-poor inserts nanometer thick layers of the interphase into the bulk crystal. This study shows that apparently conflicting results of the effect of Cu deficiency on $CuInS_2$ thin-film solar cells may be resolved by analyzing structure and composition at nanometer spatial resolution.

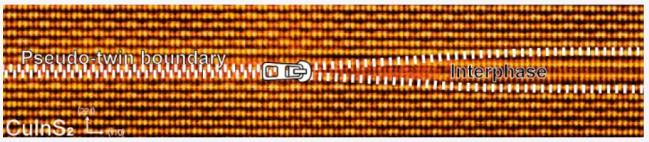

1. INTRODUCTION

1.1. $CuInS_2$ Thin-Film Solar Cells. $CuInS_2$ is a diamond-like semiconductor with the crystal structure of chalcopyrite that was first synthesized to explore the applicability to ternary compounds of the Grimm−Sommerfeld valence rules for tetrahedral coordination.[1−4] The chalcopyrites have the diamond-like zincblende structure but with two cations ordered on sublattices. The Bravais lattice of the chalcopyrite is body-centered tetragonal, belonging to space group $I\bar{4}2d$. The first crystals of $CuInS_2$ were grown to evaluate its suitability for semiconductor device applications and for its piezoelectric and nonlinear optical properties.[5−7] The direct energy band gap of $CuInS_2$ makes it a strong light absorber, with a value of 1.53 eV that lies at the optimum for efficient single-junction solar cells.[8,9] Therefore, $CuInS_2$ has been explored for polycrystalline thin-film solar cells,[10] beginning with a 3.6% efficient homojunction cell,[11] then n-CdS/p-$CuInS_2$ heterojunction solar cells first reaching 7.3%,[12] and later 11.4% power conversion efficiency.[13] What has kept the $CuInS_2$ efficiency substantially lower than the 15% reached with $CuInSe_2$ is not understood.[14] Much higher efficiencies have been reached with alloys of $CuInS_2$: 15% by alloying with Ga_2S_3 in $Cu(In,Ga)S_2$[15] and the highest efficiency achieved in any inorganic thin-film solar cell of 23.35% with a compositionally graded $Cu(In,Ga)(S,Se)_2$ alloy absorber layer.[16]

CdTe and $Cu(In,Ga)Se_2$ thin-film solar panels are deployed on large scales. The commercial successes of these solar cells made of polycrystalline thin films are the result of primarily empirical research and development. Controlling electrically active defects and carrier lifetimes remains an art. Stoichiometry, point and line defects, grain boundaries, and interfaces affect conductivity type, carrier mobility and recombination lifetime, and thereby solar cell efficiency. Overall, the

Received: September 29, 2020
Revised: November 5, 2020
Published: November 19, 2020

quantitative understanding of the electronic properties of polycrystalline thin-film compound semiconductors is far from that of polycrystalline silicon,[17,18] which grew from an exhaustive grasp of the properties of single-crystalline silicon. To the device physics community, it is a given that the quantitative understanding of single-crystal chalcopyrite semiconductors is indispensable for reaching maximum thin-film solar cell performance. Therefore, soon after initial exploration,[5−7] raising solar cell efficiency became the principal motive for studying $CuInS_2$ single crystals.[19−28] An exemplary single-crystal result is the measurement of electron mobilities as high as 338 $cm^2/(V\ s)$,[22] providing an important yardstick for assessing the device quality of polycrystalline $CuInS_2$ films. The goal of this study was to resolve a long-standing debate in polycrystalline $CuInS_2$ solar cells, namely the existence and presumed effects of Cu deficiency, by clearly identifying the phase(s) and defects in a $CuInS_2$ single crystal grown from a slightly copper-deficient melt.

1.2. Stoichiometry of $CuInS_2$. Chalcopyrite crystals can be homogeneous at nonstoichiometries of up to several atomic percentages.[1,29] A finite range of sulfur content is evident from the ability to make $CuInS_2$ crystals n-type by annealing under minimum sulfur pressure and p-type when annealed at high pressure.[6,9] That allowed the fabrication of an n- on p-type homojunction thin-film cell made by changing the sulfur pressure from high to low during film growth.[11] Indeed, adjusting composition instead of substitutionally doping remains the means of controlling carrier type and magnitude of the electrical conductivity in $CuInS_2$, but the role of Cu nonstoichiometry in setting the efficiency of polycrystalline thin-film $CuInS_2$ solar cells remains controversial. The search for high-efficiency initially explored Cu-poor material,[30] as employed in $CuInSe_2$ cells,[31] then moved to Cu-rich $CuInS_2$,[10,13,30] and then back again to Cu-poor $Cu(In,Ga)S_2$.[15] Several reports describe depositing $CuInS_2$ absorber films with excess Cu, and then removing that excess by etching in KCN solution prior to heterojunction fabrication, insinuating substantial solubility of Cu in $CuInS_2$.[10,13,30,32] A recent study illustrates the challenge of identifying the solar optimal stoichiometry of $CuInS_2$. Lomuscio et al.[32] prepared $CuInS_2$ polycrystalline films with either copper excess or copper deficiency, set by either single- or two-step vacuum deposition under five different temperature protocols. Surprisingly, the quasi-Fermi level split measured in the films (a gauge of achievable open-circuit voltage) did not correlate with the open-circuit voltage of $CuInS_2$ solar cells made from these films. The observation by Klenk et al.[10] that films with copper-poor compositions exhibit very Cu-deficient free surfaces points to the possibility of phase separation between $CuInS_2$ and a Cu-poor phase. Such phase separation may also occur at interfaces, as is suggested by the formation of a $CuIn_5S_8$ interlayer by Cu out-diffusion from a $Cu(In,Ga)Se_2$ absorber near the heterojunction into the overlaying In_xS_y buffer, which depletes the absorber of Cu.[33] By changing the energy band alignment or the conductivity type at the heterojunction, such depletion can have drastic effects on solar cell efficiency.[34−37] Therefore, to design the optimal solar cell material, it is clearly important to know where the Cu-poor boundary of $CuInS_2$ lies and what the crystal properties at that phase boundary are.

1.3. Phase Diagram of $CuInS_2$. Observations made during the first growth of single crystals[5] suggested that the tetragonal γ-phase of $CuInS_2$, which is the stable modification below 980 °C,[23,38] has a narrow homogeneity range, as was also suggested by the In_2S_3 and $Cu_{2-x}S$ admixtures detected in evaporated $CuInS_2$ thin films.[12] While Binsma et al.[38] extrapolated to a narrow Cu-rich and a wider Cu-poor homogeneity range at room temperature, in the course of a study of the In-$CuInS_2$ phase diagram Fearheiley et al.[23] found no appreciable solubility of In (suggesting no appreciable Cu deficiency) in $CuInS_2$. Verheijen et al.[39] identified a homogeneity range from 50 to 52 mol % In_2S_3 (i.e., Cu deficiency) in the $Cu_2S-In_2S_3$ binary system. Crystals grown from stoichiometric melts under temperature gradients >10 °C/cm contained lamellar structures of stoichiometric $CuInS_2$ separated by the highly Cu-deficient thiospinel $CuIn_5S_8$.[24−26,40] The authors suggest that Cu-deficient $CuInS_2$ is not stable and surmise that the formation of $CuIn_5S_8$ from stoichiometric melts indicates that constitutional supercooling is enabled by the dissolution of Cu_2S in $CuInS_2$ (i.e., $CuInS_2$ can absorb excess Cu_2S). The summary of this group of investigations is that stoichiometric $CuInS_2$ can take up Cu_2S but not lose it. A crystallographic study of the compositions of polycrystalline films in the $Cu_2S-In_2S_3-Ga_2S_3$ ternary system with focus on Cu-poor compositions[41] also concluded that the Cu-poor homogeneity range must be very narrow; all Cu-poor compositions did result in two-phase mixtures of essentially stoichiometric $CuInS_2$ and $CuIn_5S_8$.[42−44]

A detailed theoretical study of point defects in $CuInSe_2$ by density-functional theory by Zhang et al.[45] suggests that Cu deficiency is accommodated by the formation of stable, electrically neutral $[V_{Cu}^{1-}In_{Cu}^{2+}V_{Cu}^{1-}]$ defect triplets; these enable the self-compensation of Cu vacancy acceptors, V_{Cu}, by moving In to Cu sites where it becomes the antisite donor In_{Cu}. The defect triplets are the basic structural constituent of group I deficient ordered defect compounds (ODC). Wasim et al.[46] verified these theoretical findings with a combined experimental and theoretical study of a group of chalcopyrites and their ODC derivatives. It is important to keep in mind that Cu deficiencies introduced in phase diagram studies, or in crystal and thin-film growth, are large by the standard of electronic substitutional doping. While a 1 at. % deficiency in composition may produce mostly electrically neutral defects like $[V_{Cu}^{1-}In_{Cu}^{2+}V_{Cu}^{1-}]$, it still might leave a minor (e.g., 10^{-4} at. %) concentration of electrically active dopant defects, enough to dominate charge transport in solar cells.

In this study we identify the phase(s) as well as the structural and the optoelectronical properties of a $CuInS_2$ crystal grown from a 1 mol % Cu-deficient melt. We describe crystal growth and basic crystal properties and then the crystal's atomic structure as seen by scanning/transmission electron microscopy (STEM), plus its fine structure atomically mapped in conjunction with atomic scale electron dispersive spectroscopy (EDS) for analysis of composition. The crystal's optoelectronic properties are evaluated by measuring electronic transport and photoconductivity. The results are fascinating: we discovered a Cu-deficient phase *in statu nascendi*, including the gradual displacement of In from its normal site in the chalcopyrite to a new site that, while interstitial in the chalcopyrite, is the dominant position of In in the Cu-deficient phase.

2. INSTRUMENTATION AND METHODS

Powder X-ray diffraction analysis was performed on a Bruker D8 Advance Eco with Cu Kα radiation and a LynxEye-XE detector. The scan parameters were 0.02°/step with 0.085 s/

https://dx.doi.org/10.1021/acs.jpcc.0c08872
J. Phys. Chem. C 2020, 124, 26415−26427

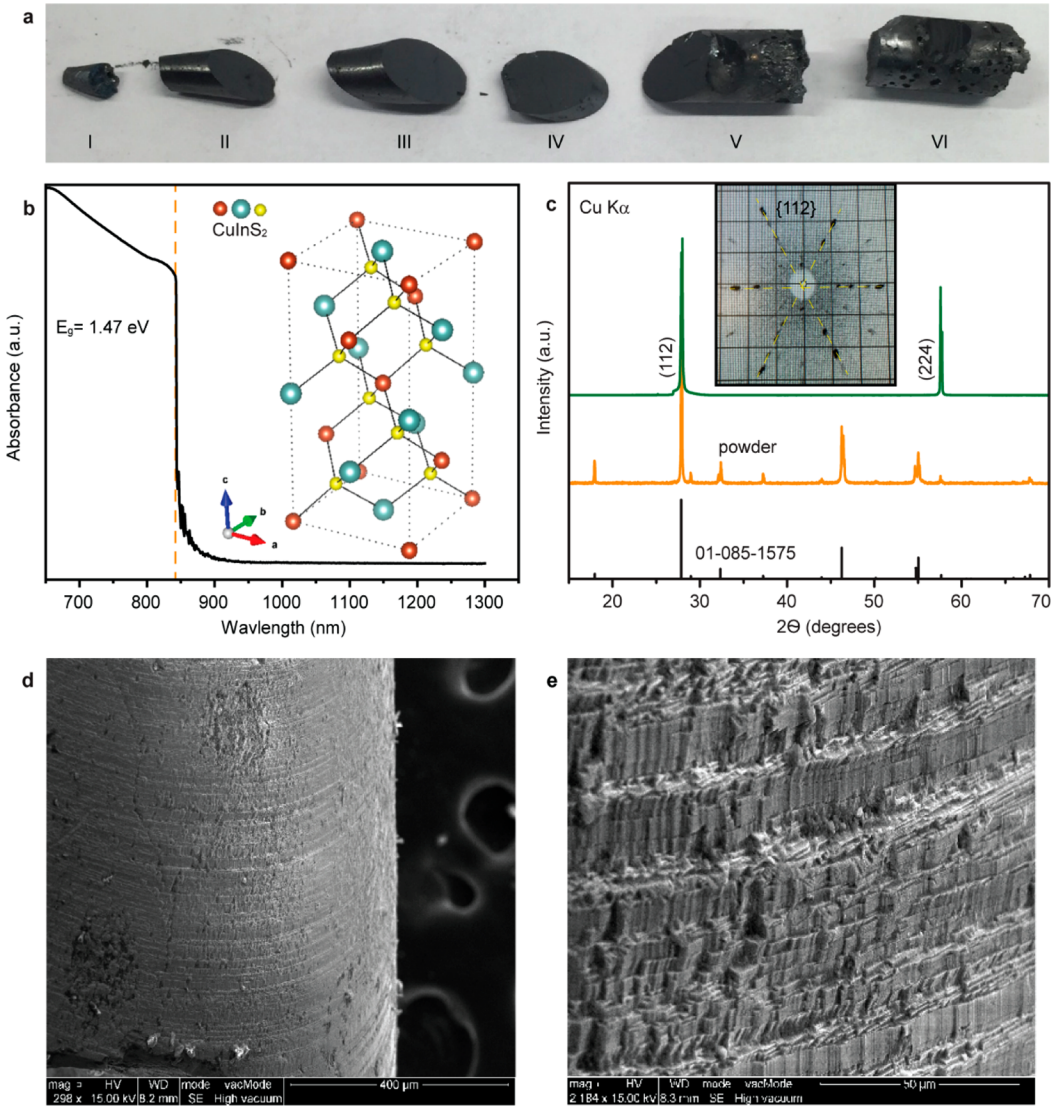

Figure 1. Structural and optical characterization of 1 mol % Cu-deficient $CuInS_2$ single crystal. (a) The single-crystal boule cleaved along the (112) in six sections upon extraction from the growth ampoule. All measurements in this work were performed on crystals extracted from section IV. (b) Optical absorption spectrum of $CuInS_2$, showing a sharp onset of absorption at 1.47 eV. A freshly cleaved (112) slab (0.3 mm thick) was exposed for this measurement. The inset shows the tetragonal chalcopyrite structure of $CuInS_2$. (c) XRD pattern of the single crystal face (green), powder form (orange), and database pattern match (black). The inset shows a Laue diffraction pattern of the (112) crystal surface. SEM imaging of section IV is presented at magnifications of (d) 250× and (e) 2000×, revealing the pronounced (112) terraces on the perimeter of the crystal boule.

step, for a total scan time of 8 min. A Quanta 200 field emission gun environmental scanning electron microscope (SEM) equipped with an integrated Oxford System was employed for energy dispersive X-ray (EDS) analysis, for routine evaluation of chemical constituents. X-ray photoelectron spectra (XPS) were collected under 10^{-9} Torr by using a ThermoFisher K-Alpha X-ray photoelectron spectrometer. All spectra were recorded by using Al Kα radiation (1487 eV) with a survey and pass energy of 100 and 20 eV, respectively. Measured peaks were fit by using Casa XPS software and a Shirley background. The C 1s peak at 284.5 eV of adventitious hydrocarbon was used as an internal binding energy reference. The optical bandgap was measured with an Agilent Technologies Cary 5000 UV−vis−NIR spectrometer equipped with a Universal Measurement Accessory (UMA) with incident light from 200 to 1300 nm wavelength.

Photoconductivity measurements were performed on the same instrument as the electronic transport measurements, a Quantum Design Physical Property Measurement System, using a custom dark-room setup. Ohmic contact was made with Pt wires connected to the (112) surface with an InGa eutectic. Current−voltage curves were plotted in real time as the potential was swept between −10 and 10 V at varying LED light intensities with each wavelength tested (365, 395, 462, 537, 640, 780, 850, 940, and 1050 nm). These measurements were performed at room temperature.

The resulting symmetric $I-V$ curves demonstrate ohmic behavior, verifying that non-ohmic contacts are not the origin of the observed effects. The linear slope of the $I-V$ curves indicates that the system's free electron lifetime remains constant, given the relationship $I = e\frac{F\mu\tau}{L^2}V$, where e is the electron charge, F is the free electron generation rate, μ is the mobility, τ is the free electron lifetime, and L is the spacing of electrodes.

https://dx.doi.org/10.1021/acs.jpcc.0c08872
J. Phys. Chem. C 2020, 124, 26415−26427

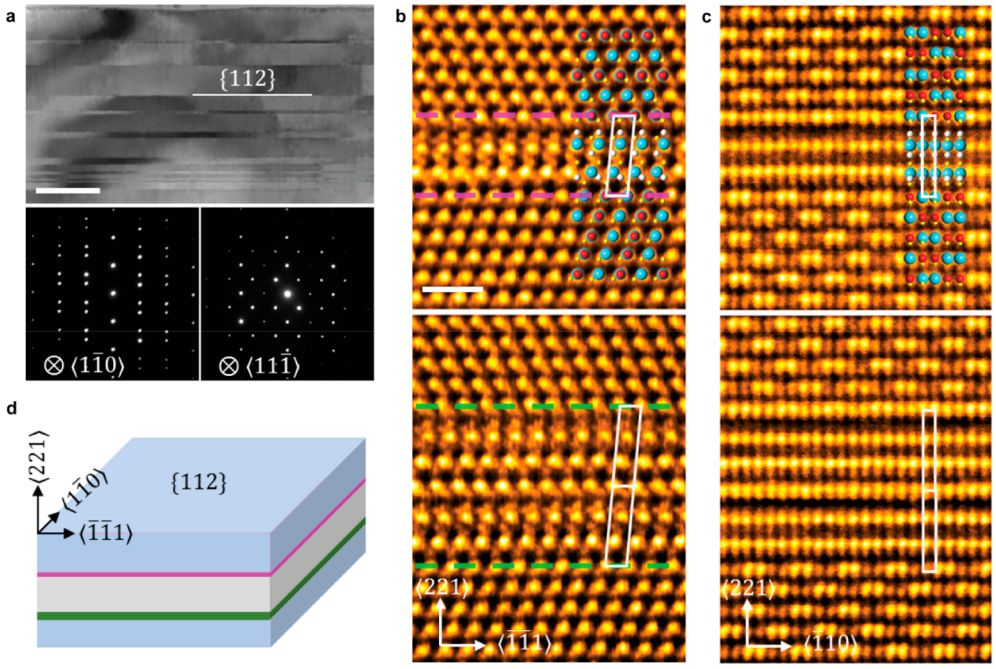

Figure 2. Microstructure of chalcopyrite $CuInS_2$. (a) Bright-field TEM image showing lamellar pseudotwins. The pseudotwin plane is {112}. Scale bar: 500 nm. The corresponding composite diffraction patterns of the bottom panels were taken along the ⟨1$\bar{1}$0⟩ and ⟨$\bar{1}$11⟩ zone axes, respectively. (b, c) High-resolution STEM HAADF images showing parts of chalcopyrite $CuInS_2$ pseudotwins above and below single (top frames) and double layers (bottom), viewed from the ⟨1$\bar{1}$0⟩ and ⟨$\bar{1}$11⟩ directions, respectively. A color-coded chalcopyrite structure (Cu, red; In, blue; S, yellow) is overlaid on the TEM images to identify atoms. In (c), atomic-column pairs of Cu and In can be seen—note the alternation of bright (In) and faint (Cu) pairs in the bulk crystal. Scale bar: 1 nm. (d) Schematic illustration of (blue or gray) bulk $CuInS_2$ pseudotwin lamellae separated by a single (magenta) and a double (green) interphase, all stacked in the ⟨221⟩ direction.

3. EXPERIMENTAL RESULTS

3.1. Single Crystal Growth and Initial Characterization. Polycrystalline $Cu_{0.99}In_{1.00}S_{2.00}$, (i.e., 1 mol % Cu deficient) was synthesized from the elements Cu (99.99%), In (99.999%), and S (99.99%) in an evacuated quartz tube at T = 1100 °C.[47] After ascertaining the chalcopyrite structure by powder X-ray diffraction (XRD) and composition by EDS, ∼20 g was ground into large grains and sealed under vacuum in a carbon-coated quartz tube. The $CuInS_2$ single crystal was grown in a vertical Bridgman furnace set to 1140 °C. The quartz tube was held in the hot zone for 24 h and then lowered through the length of the furnace at 0.1 mm/h, and finally annealed at T = 400 °C for 24 h. This annealing temperature approximates the substrate temperatures in films deposited by thermal evaporation of the elements.[32,41] The four independent variables—stipulated by the phase rule for setting the composition of a ternary compound—are temperature, total pressure, sulfur partial pressure, and copper-to-indium ratio.[23,48−50]

During extraction from the quartz tube, the 38 mm long single crystal ingot cleaved along the (112) plane into six pieces (Figure 1a). All further measurements were made on the section IV piece, ∼14 mm from the tip of the ingot. Four different samples were cleaved for evaluating optical, X-ray, TEM, and photoconductivity characteristics. The freshly cleaved samples were not chemically etched prior to measurement. The material's optical transmission spectrum (Figure 1b) exhibits the steep absorption edge of a direct-gap semiconductor, from which we extract an optical band gap of 1.47 eV. Figure 1c shows the XRD patterns of the (112) face of a $CuInS_2$ crystal and of a powder sample prepared from the crystal boule and the corresponding database pattern. The diffraction lines are not broadened, as they might be by small domains. Laue diffraction identifies the crystal's natural cleavage plane as (112) (inset to Figure 1c), and powder XRD confirms the tetragonal chalcopyrite structure (space group $I\bar{4}2d$). XPS confirmed Cu^{1+} and In^{3+} oxidation states as well as an S^{2-} sulfide peak (Figure S1). With SEM we found that the crystal's perimeter—which had been in contact with the carbon-coated quartz wall—exhibits pronounced (112) terraces, that is, along the natural cleavage plane (Figure 1d,e).[23]

3.2. Microstructure of the Bulk Chalcopyrite $CuInS_2$. Samples for transmission electron microscopy were prepared by focused ion beam cutting in a FEI Helios NanoLab 600 dual-beam system (FIB/SEM). Conventional TEM imaging, atomic resolution high-angle annular dark-field (HAADF) scanning transmission electron microscopy (STEM) imaging, and atomic-level EDS mapping were performed on a double Cs-corrected FEI Titan Cubed Themis 300 scanning/transmission electron microscope (S/TEM) equipped with an X-FEG source operated at 300 kV and a Super-X EDS system. Relative compositions were determined with EDS by integrating the area of the elemental peaks. The stated compositions are average values over selected areas or pixels (making image resolution important); their estimated accuracy is ±0.5 at. %. The TEM elemental signal at a given atom position is produced by a whole column of atoms that are superposed in the ∼100 nm thick sample. Therefore, the signal intensity combines the electron density (Z number) of the particular atom (or atoms when viewing in directions where Cu and In are superposed; see Figure 4c) with the occupation of the column. While the EDS signal does not directly tell us the number of occupied sites in an atomic column, line scans

https://dx.doi.org/10.1021/acs.jpcc.0c08872
J. Phys. Chem. C 2020, 124, 26415−26427

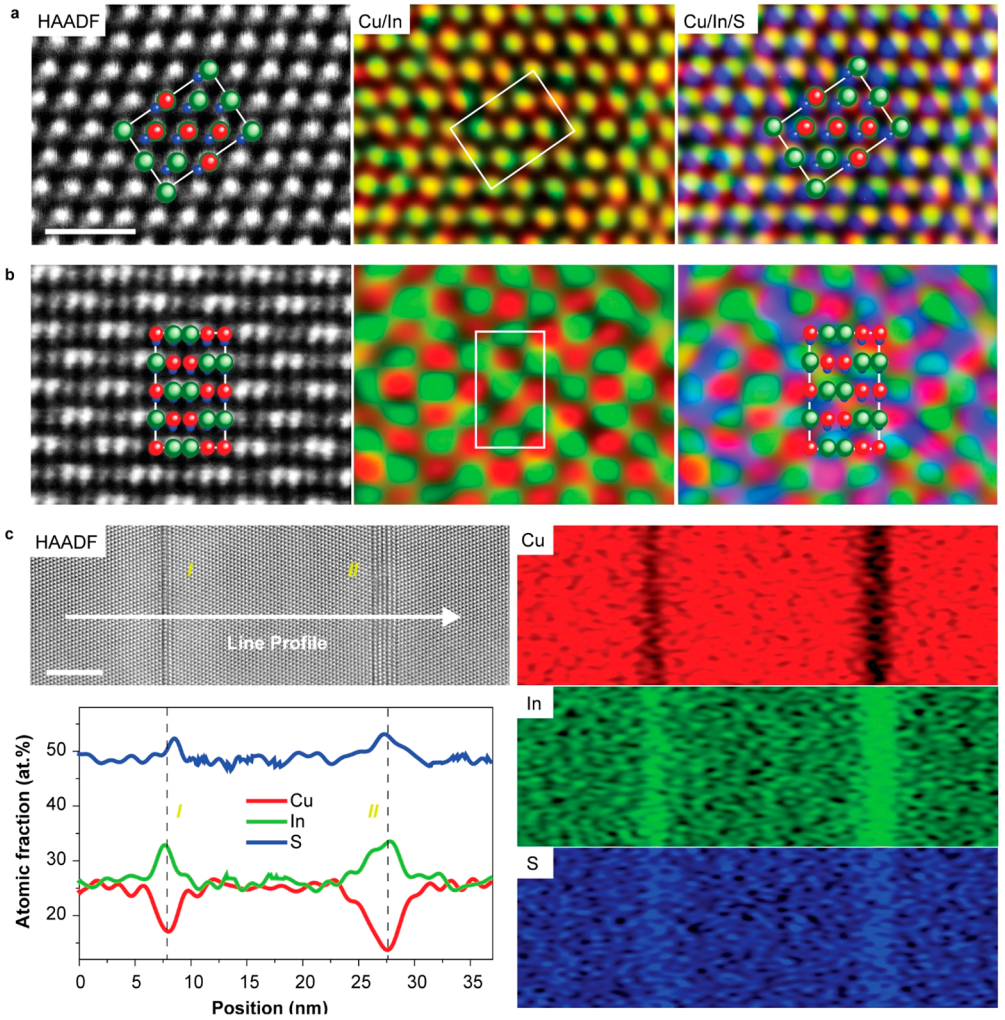

Figure 3. Quantitative analysis of composition. (a, b) Atomic-level STEM-EDS maps showing the positions of Cu (red), In (green), and S (blue) in bulk chalcopyrite $CuInS_2$. The top row is viewed along the $\langle 1\bar{1}0\rangle$ direction and the second row along $\langle \bar{1}11\rangle$. The leftmost panels show HAADF-STEM images, the center panels the element mappings of Cu/In, and the right panels of Cu/In/S. The chalcopyrite unit cell is delineated to highlight the positions of the three elements. In the $\langle 1\bar{1}0\rangle$ projection Cu and In atoms are superposed; in the $\langle \bar{1}11\rangle$ projection they are separate. Scale bar: 1 nm. (c) STEM-EDS mapping of bulk $CuInS_2$ including one pseudotwin boundary with a single (I) and one with a double (II) interphase layer. The HAADF image shows the EDS trace across the bulk and the two interphases. The right panel combines the elemental maps of Cu (red), In (green), and S (blue) from multiple scans. The compositional profiles along a single scan, at the bottom left, show Cu depletion and In and S enrichment in the interfacial layers. Scale bar: 5 nm. To improve the contrast in elemental maps, color coding in this figure, and in Figures S2 and S3, is red/green/blue, different from the red/blue/yellow in Figures 1, 2, 4, and 5.

or area scans do trace *changes* in occupation and hence composition; maximal intensity reflects complete occupation of a column, as in bulk $CuInS_2$.

The TEM image in Figure 2a taken in the $\langle 1\bar{1}0\rangle$ direction shows that the $CuInS_2$ crystal has a lamellar structure. The lamellae are alternating pseudotwins that form a herringbone pattern. The thickness of the lamellae ranges from several nanometers to hundreds of nanometers. The corresponding composite diffraction patterns from the pseudotwins are shown in the bottom panels of Figure 2a. They are taken from the $\langle 1\bar{1}0\rangle$ and $\langle \bar{1}11\rangle$ zone axes, respectively, and identify the pseudotwin plane as {112}. The pseudotwins are separated by a rotational-twin boundary (a 180° rotation)[24] that has been theorized to be the most energetically favored twin boundary in chalcopyrites, as it avoids the reconstruction that would be inevitable in anion- and cation-terminated twin boundaries.[51,52] Pairs of twins are imaged at the tops and bottoms of each frame of Figure 2b,c.

Periodic interfacial structures ("interphases") are seen to be inserted into the pseudotwin boundaries. In Figure 2b,c these structures are viewed by aberration-corrected STEM from the $\langle 1\bar{1}0\rangle$ and $\langle \bar{1}11\rangle$ directions, respectively. The interphases at the pseudotwin boundaries, shown schematically in Figure 2d, contain a single (top frames of Figure 2b,c) or a double (bottom frames) layer. In Figure 2c the bulk chalcopyrite exhibits alternating pairs of bright (In stack) and faint (Cu stack) spots. As seen in the top frames, the single-layer interfacial structure includes two bright atomic planes but with interplanar spacings different from those of the chalcopyrite $CuInS_2$ bulk. The bulk twins sandwich the interfacial phase. Note, again, that in the atomic resolution images changes in spot size or intensity reflect changes of the type and/or the number of atoms in the stack at that position.

3.3. Composition of Bulk Crystal and of Interfacial Structures. The chemical compositions of bulk and interphases were determined by mapping the three elements

https://dx.doi.org/10.1021/acs.jpcc.0c08872
J. Phys. Chem. C 2020, 124, 26415−26427

by atomic-level STEM energy-dispersive X-ray spectroscopy. Figure 3a,b shows STEM-HAADF images of bulk chalcopyrite $CuInS_2$ and the corresponding elemental maps of Cu (red), In (green), and S (blue), viewed along the $\langle 1\bar{1}0\rangle$ and $\langle \bar{1}\bar{1}1\rangle$ directions, respectively (see more details of single-element mappings in Figure S2). The bulk composition is 25.2 at. % Cu, 24.3 at. % In, and 50.5 at. % S (Table S1), which is, within accuracy, the stoichiometry of $CuInS_2$. The chalcopyrite unit cell is delineated to identify the atomic positions. While in the $\langle 1\bar{1}0\rangle$ projection (Figures 3a and 4c) Cu and In atoms lie on top of each other, in the $\langle \bar{1}\bar{1}1\rangle$ projection of Figure 3b they alternate (bright, In; weak, Cu).

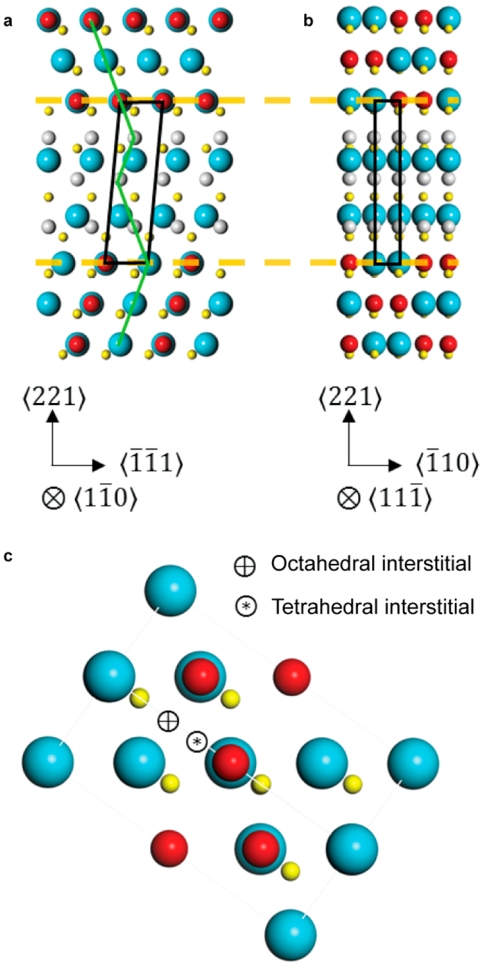

Figure 4. Schematic of the interfacial structure. (a, b) Atomic model of the single-layer interfacial structure (top frames of Figure 2b,c) viewed along the $\langle 1\bar{1}0\rangle$ and $\langle \bar{1}\bar{1}1\rangle$ zone axes, respectively. (c) Chalcopyrite unit cell viewed in the $\langle 1\bar{1}0\rangle$ direction, identifying the interstitial sites. Note the overlaid Cu (red) and In (blue) positions. The ball size qualitatively reflects the Z (= electron) number of a given atom.

We used EDS to also determine by how much the composition of the interphases deviates from bulk $CuInS_2$ along the trace marked in the HAADF image of Figure 3c. The panel at its right shows the element maps of Cu (red), In (green), and S (blue). The lower left panel shows the EDS-determined concentration profiles along the trace in the STEM-HAADF image above. With respect to the bulk, the interfacial layers are depleted of Cu (down −7.9 at. % in the single layer and down −11.5 at. % in the double layer) and contain up to +8.6 at. % excess In and +3.0 at. % excess S. Thus, while the bulk contains 25.2 at. % Cu, the single and double interfacial phase layers contain only 17.1 and 13.7 at. % Cu, respectively, but 32.9 at. % In (for sulfur see Table S1). An additional example, analyzed along the $\langle \bar{1}\bar{1}1\rangle$ direction, is provided in Figure S3. The copper deficiency of the interfacial phase suggests that the interfacial phase accommodates the copper deficiency of the overall crystal.

3.4. Structure of the Cu-Deficient Interphases and the $[V_{Cu}In_iV_{Cu}]$ Triple Point Defect. The atomic occupations in the interfacial structures can be deduced from the atomic resolution STEM-HAADF images of Figure 2b,c. Figure 4 shows the corresponding atomic models of a single-layer interfacial structure (top frames of Figure 2b,c), viewed from $\langle 1\bar{1}0\rangle$ and $\langle \bar{1}\bar{1}1\rangle$, respectively. Note the color codes in Figures 4 and 5, where In is coded blue and S yellow throughout; the Cu position, however, is coded red in the chalcopyrite structure but gray in the interphase, the latter because we cannot exclude partial occupation by In. In Figure 4a, viewed along the $\langle 1\bar{1}0\rangle$ direction, Cu and In overlap in the chalcopyrite bulk structure, as further illustrated in the unit cell of Figure 4c. Viewed along $\langle \bar{1}\bar{1}1\rangle$ in Figure 4b, the Cu and In positions are separate. The black quadrangles in Figure 4a,b delineate the minimal cells of the interphase structures.

Because the atom positions in the interphases are largely derived from those in the bulk, we turn to inspecting the STEM-HAADF image of Figure 5 taken along the $\langle 1\bar{1}0\rangle$ zone axis (see Figure 4a). Figure 5 shows a transition from a pseudotwin boundary in the bulk, at left, to a single-layer interphase. Three In rows of the chalcopyrite bulk are seen to merge into two rows (blue) in the interphase. There, one row lies at the normally occupied chalcopyrite site In_{In} (e.g., 1/4, 1/4, and 1/8). The other row of In is positioned as interstitial In_i at tetrahedral interstices (e.g., 3/4, 1/4, and 1/8) in the chalcopyrite structure, identified in Figure 4c. The additional occupation of tetrahedral sites forms an In-enriched interfacial layer. While in the transition from bulk to interphase the Cu atoms remain in their bulk Cu_{Cu} positions, Figure 5a shows that their intensity fades in the transition from left to right. To remind the reader that in the interphase these positions remain normal Cu-on-In stacks (instead of Cu only) they are color-coded gray. However, their intensity becomes so small that we can be certain that in going from the bulk to interphase many Cu_{Cu} sites in the stack are emptying out and become copper vacancies, V_{Cu}. Note that as Cu fades, the In intensity increases going from left to right, a consequence of the merger of three rows in the bulk to two rows in the interphase. Thus, a dominant feature of the interphase is a fully occupied In stack (blue) placed between two stacks that, given their faint intensity, are highly deficient in Cu (gray). In the interphase, the EDS concentrations of Figure 3c go down to a Cu deficiency of 11.5 at. % and up to an In excess of 8.6 at. %. Hence, the estimated atomic ratio of V_{Cu} to In_i is 11.5/8.6 = 1.34. Taken together, the atomic positions of two faint Cu stacks sandwiching the In_i stack, plus this ratio 1.34, are structural and compositional indicators for a high concentration of $[V_{Cu}In_iV_{Cu}]$ defect triplets. In_{In} is an electron donor, and V_{Cu} is an electron acceptor. The defects will exchange charge, such that $[V_{Cu}In_iV_{Cu}]$ triplets self-compensate to electrically neutral $[V_{Cu}^{1-}In_i^{2+}V_{Cu}^{1-}]$.

The crystal contains planar, line and point defects. The interphase introduces a defect plane. This plane becomes apparent when counting from the meeting point of the

https://dx.doi.org/10.1021/acs.jpcc.0c08872
J. Phys. Chem. C 2020, 124, 26415−26427

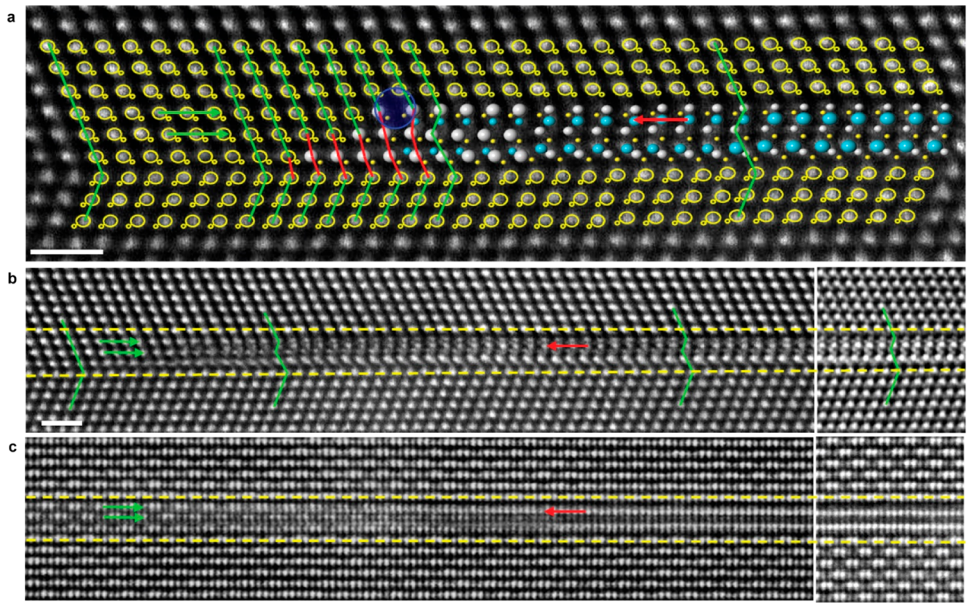

Figure 5. Transition from pseudotwin boundary to interphase, observed going from left to right. (a) Magnified STEM-HAADF image along the $\langle 1\bar{1}0 \rangle$ zone axis, with an overlaid atomic model to highlight the interfacial defect formed by the pseudotwin boundary. The big and small open circles in the $CuInS_2$ bulk structure represent the occupations of Cu/In and S, respectively (see Figure 2b). The In (blue) and S (yellow) atoms located in the interphase layer are color-coded as in Figures 1a, 2b,c, and 4. Cu is shown in gray (see text). The chalcopyrite phase at left has In and Cu atoms that lie on top of each other in their normal positions (gray). Going to the right, one can see that In (blue) has emerged from that stack by moving to a new position, which is the tetrahedral interstitial site of chalcopyrite. (b, c) Original STEM-HAADF images, viewed along the $\langle 1\bar{1}0 \rangle$ and $\langle \bar{1}\bar{1}1 \rangle$ zone axes, showing how the interphase emerges from the pseudotwin boundary. Sectioned off at right are images taken far from this transition. Scale bars: 1 nm.

herringbone pseudotwin lattice planes in the bulk (green lines with elbows at the left of Figure 5a and b) to equivalent planes separated by the interphase. There the equivalent bulk planes are offset, as illustrated in Figure 5a,b (and Figure 4a) by the jogs in the green lines that run from bulk to bulk across the interphase. This slip plane constitutes a planar defect that is contained in the interphase.

The transition from or to the pseudotwin plane to interphase produces a line defect, which in Figure 5a is surrounded by the blue circle. This is a partial dislocation, $1/6\ \langle \bar{1}\bar{1}1 \rangle$, which is similar to the $1/6\ \langle 112 \rangle$ in the face-centered cubic system. This dislocation compensates the displacement of interfacial atoms that is traced by the red lines. The blue circle around the positions of the atoms that surround the dislocation draws attention to the mispairing of coordinative bonds caused by the change of atomic stacking. As seen in Figure S4, some of the interlayer phases form disks that are fully embedded in the crystal (instead of running from side to side) and therefore will be surrounded by a ring of these partial dislocations.

Thus, structural defects include the (112) pseudotwin boundary of the bulk crystal, the (112) slip plane within the interphase, the $1/6\ \langle \bar{1}\bar{1}1 \rangle$ partial dislocation at the perimeter of the interphase, and In_i and V_{Cu} within the interphases. What are their optoelectronic consequences?

3.5. Electronic Transport and Photoconductivity. Electronic transport properties were measured along the (112) plane of a $2 \times 3 \times 0.3\ mm^3$ sample with eutectic In−Ga contacts made on the (112) surface and Pt lead wires by using a PPMS. In-plane resistivity vs temperature data (plotted in Figure 6) were collected from 395 to 300 K—where we reached the measurement limit of our equipment. At $T = 300$ K, ρ_{xx} is $2.7 \times 10^6\ \Omega$·cm. From plotting $\log(\rho_{xx})$ vs $1/T$ (inset, Figure 6a) we extract the thermal activation energy of 87 meV. Hall effect measurements performed at magnetic fields from $\mu_0 H = -3$ to 3 T at 300 K gave the Hall resistivity ρ_{xy}, shown in Figure 6b. The actual quantity plotted is ρ_{xy} with some admixture of ρ_{xx} because the Hall contacts were not made exactly orthogonal to the current and field directions. The negative slope reflects n-type conduction. The calculated electron concentration, n, is $2.3 \times 10^{13}\ cm^{-3}$, and the electron mobility, μ_n, calculated from ρ_{xy} and n, is 0.1 $cm^2\ V^{-1}\ s^{-1}$. While high ρ and low n have been observed before, μ_n is unusually low.[6,9] Given that the (112) interphase layers embedded in the crystal may cause anisotropic conduction, we made a top-to-bottom ([112] direction) resistance measurement, from which we estimate $\rho_{zz} \approx 1 \times 10^6\ \Omega$·cm, i.e., close to the ρ_{xx} measured laterally.

Photoconductivity was measured in the configuration shown in the inset to Figure 7a, with InGa eutectic and Pt wire contacts applied to the (112) face of the sample that had been characterized by TEM. LEDs of the eight different wavelengths (ThorLabs, FWHM ≈ 55 nm) shown in Figure 7a illuminated the sample at irradiances ranging from 0.25 to 70 mW/cm^2, over voltages from ±10 V supplied by the PPMS. Illumination with LEDs enables high irradiance at the expense of modest spectral resolution. Irradiances were measured by using a digital hand-held optical power meter (model PM100D, Thorlabs) coupled with a photodiode power sensor (model S120VC, Thorlabs).

In the responsivity vs wavelength graph of Figure 7a, for applied voltages ranging from 1 to 10 V, dotted lines serve as guides for the eye. The responsivity peaks at 780 nm, corresponding to a photon energy of 1.59 eV (±0.05 eV LED FWHM). The linear decrease in responsivity with wavelengths below 780 nm reflects a constant quantum efficiency. While Figure S5 shows the photocurrent vs voltage

https://dx.doi.org/10.1021/acs.jpcc.0c08872
J. Phys. Chem. C 2020, 124, 26415−26427

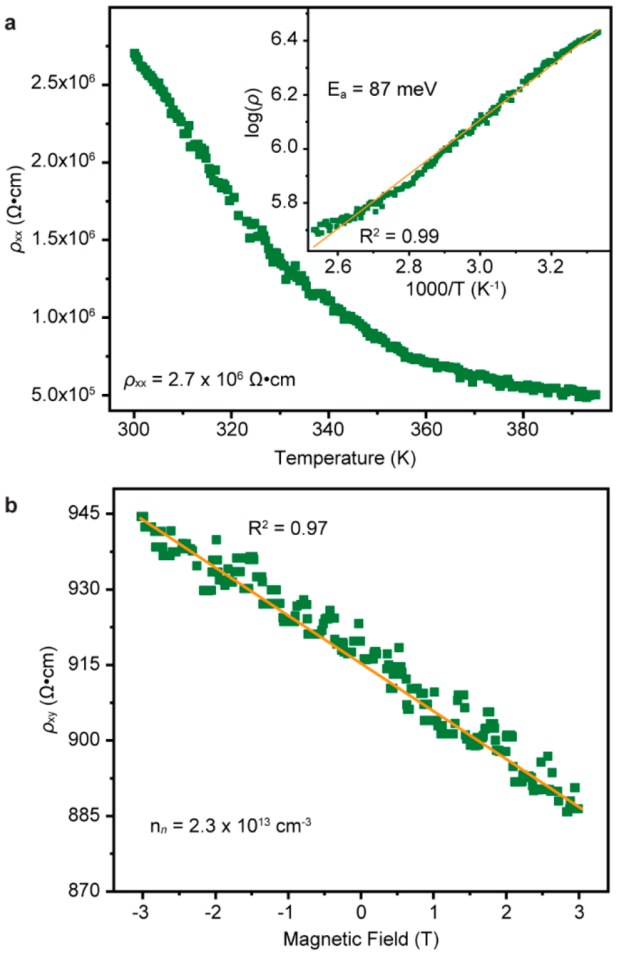

Figure 6. Electrical characterization of the 1 mol % Cu-deficient $CuInS_2$ single crystal. (a) Resistivity (ρ_{xx}) vs temperature profile from 300 to 395 K. The inset plots this data as log ρ_{xx} vs $1/T$ from which an activation energy of 87 meV is extracted. (b) Hall resistivity (ρ_{xy}) vs magnetic field from $\mu_0 H = -3$ to 3 T at 300 K. The negative slope identifies electrons as the crystal's majority carrier. From this data we can calculate an electron concentration, n, of 2.3×10^{13} cm^{-3}.

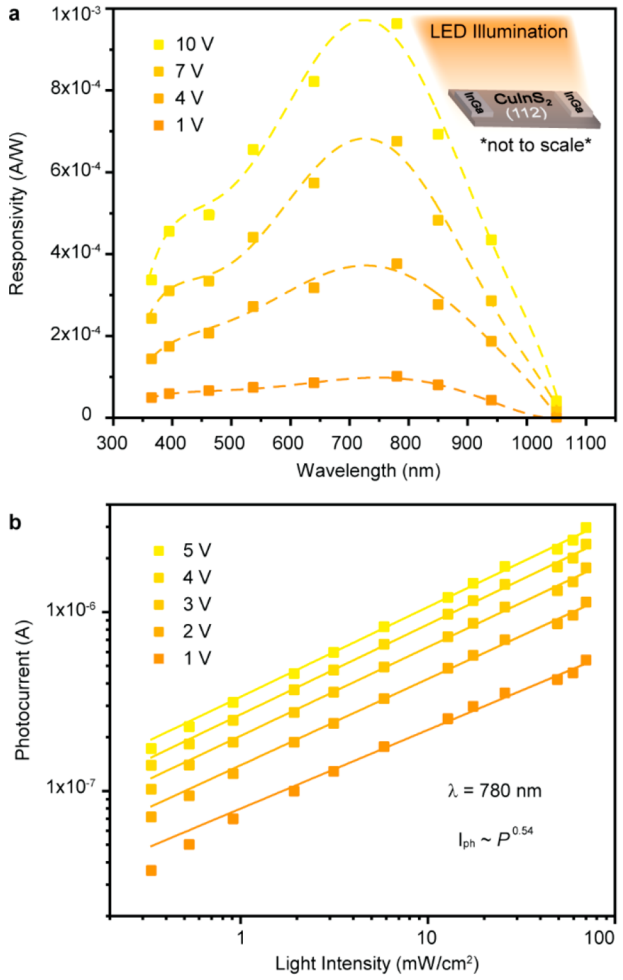

Figure 7. Photoelectric properties of the $CuInS_2$ crystal. (a) Responsivity vs wavelength for four applied voltages. The responsivity is highest at 780 nm. The inset shows the measurement geometry. (b) Photocurrent vs light intensity at 780 nm illumination for five applied voltages. A simple power law fit (solid lines) results in an exponent of 0.54.

plot for 780 nm irradiance from 0.25 to 70 mW/cm^2, Figure 7b shows the log–log plot of the photocurrent vs 780 nm irradiance. The dependence of log photocurrent on log light intensity is linear and fits a simple power law: $I_{ph} = AP^{\alpha}$, where I_{ph} is the photocurrent, A is a scaling constant, P is the irradiance, and α is an exponent. The solid lines represent this fit. The slopes of these fits for 2–5 V applied bias are identical at $\alpha = 0.54$.[53]

4. DISCUSSION

4.1. [$V_{Cu}In_iV_{Cu}$] Triple Point Defect. Electron microscopy of structure and composition at atomic resolution shows that introducing Cu deficiency in a $CuInS_2$ crystal results in exactly stoichiometric $CuInS_2$ bulk with intercalated sheets of a phase that is highly Cu-deficient and In-rich. These interphases lie in (112) planes, are nanometers thick, and contain either two or four In layers. Analysis of the transition from chalcopyrite-type bulk $CuInS_2$ to the interphase shows that three (or six) In_{In}-containing layers from normal sites in the bulk merge to two (or four) layers of interstitial In_i in the interphase, while the positions and number of the three (or six) corresponding Cu and S containing layers are preserved in the transition from bulk to interphase. There, the positions of Cu_{Cu} (and therefore V_{Cu}) on normal sites bracket interstitial In_i atoms. While the atomic positions in Figure 5 do not reveal the actual occupation of sites within each stack, Coulombic attraction will make two V_{Cu}^{1-} become nearest neighbors of one In_i^{2+}. This positioning, the estimated Cu_{Cu}, V_{Cu}, and In_i concentrations, and the high electrical resistivity of the sample taken together are conclusive indicators for the existence of electrically neutral [$V_{Cu}^{1-}In_i^{2+}V_{Cu}^{1-}$] triplets.[45] These are the basic structural modifier of ordered defect compounds in I–III–IV_2 diamond-like semiconductors. The pronounced separation into stoichiometric $CuInS_2$ and a highly Cu-deficient interlayer phase confirms that the Cu-deficient phase has high thermodynamic stability with respect to bulk $CuInS_2$. The cause of this stability is the reduction of Cu content, which diminishes the intensity of repulsion by the antibonding Cu d–S p hybrid states that form the top of the valence band.

A rough estimate suggests that the interphase layers absorb much of the Cu deficiency introduced with the initially Cu-deficient charge used for crystal growth. Viewing the excess In in the interphases as the binding agent for Cu vacancies that

https://dx.doi.org/10.1021/acs.jpcc.0c08872
J. Phys. Chem. C 2020, 124, 26415–26427

have diffused out from the bulk $CuInS_2$, we calculate the concentration of V_{Cu} as approximately twice that of excess In. EDS measures that the interphase with two rows of In contains 8.6 at. % excess In. This corresponds to (2 rows) × (2 V_{Cu} per In_i) × 8.6 at. % excess $In_i \cong$ 34 at. % of Cu missing from that interphase. The interphase accommodates three rows of Cu, just like the bulk. Therefore, the overall Cu deficiency in the interphase is 3 × 34 at. % = 102 at. %, equivalent to about one row of V_{Cu}. The average thickness of bulk $CuInS_2$ between the interphase layers is ∼100 nm, which corresponds to ∼300 layers of atoms. Following this argument, the original fraction of Cu vacancies in the hypothetical homogeneous, non-stoichiometric crystal would have been ∼1/300 ≅ 0.003, a value close to the targeted Cu deficiency of 1 mol % [0.25 − 0.003 = 0.247 at. %] of the starting material. This approximate agreement suggests that excess In_i is a titer for V_{Cu} and that the interphases efficiently soak up V_{Cu} where they are thermodynamically quite stable.

Under the electron beam, the edge of an embedded interphase can be moved back and forth like a zipper. That observation implies fast movement of atoms. When zipping to extend the interphase, two rows of In_i can revert to three rows of In_{In} with minimal atomic displacement. S stays in its normal sites, as does Cu. However, a newly extended perimeter of the interphase needs stabilization by Cu vacancies. The observed zipper-like fluidity implies that V_{Cu} are supplied rapidly from the depth of the interphase to its growing edge. The electron beam likely provides the energy needed to dissociate the $[V_{Cu}^{1-}In_i^{2+}V_{Cu}^{1-}]$ triplets, thereby supplying V_{Cu} to the advancing edge. Because of the high V_{Cu} concentration, Cu_{Cu} atoms will move easily between the Cu sites, perhaps even functioning as a (112) confined sheet of Cu_{Cu} "liquid". Similarly, illumination has been observed to render $[V_{Cu}^{1-}In_{Cu}^{2+}V_{Cu}^{1-}]$ triplets in $CuInSe_2$ nanocrystals highly mobile.[54]

4.2. Crystallographic Defects. While the existence of the $[V_{Cu}^{1-}In_i^{2+}V_{Cu}^{1-}]$ triplet is made certain by a group of observations that prove the existence of a high concentration of V_{Cu} at the appropriate positions in the interphases, several crystallographic defects can be seen directly. They include the pseudotwin boundary in the (112) planes, separating lamellae of $CuInS_2$ that are rotated 180° against their neighbors; 1/6 $\langle\overline{1}11\rangle$ partial dislocations that accommodate a bond mismatch at the periphery of the embedded interphase layers; and a one-bond offset with respect to the bulk, of lattice planes that terminate at interphase layers. Typically, such planar and line defects cause electronic defects, and indeed many point defects have been postulated for $CuInS_2$.[45,55−61] While no specific electronic defect has been identified in this study, the observed photoconductivity exponent of 0.54 suggests that electronic defect levels do exist in the energy band gap, with a density of defect states decaying away from the band edges.[53,62] For a comprehensive overview of point defects in a chalcopyrite, the reader is referred to the discussion of $CuInSe_2$ by Zhang et al.[45]

The fully embedded interphase (Figure S4) demonstrates that pseudotwin boundaries do exist in the absence of interphases. This suggests that at least some, and possibly all, of the interphases did form following the growth of a nonstoichiometric crystal. While Figure 5 shows that the excess In in the interphases can be supplied by the merger of three In layers in bulk $CuInS_2$ to two layers in the interphase, V_{Cu}, however, must collect in the interphase by diffusion from the surrounding bulk. Figure 2a shows that the pseudotwin boundaries, where the interphases are located, are spaced ∼100 nm apart. It is instructive to compare the diffusion lengths of Cu and In under the crystal's annealing conditions of 400 °C for 24 h because that is the lowest temperature at which a solid-state reaction might have proceeded in the present crystal. The diffusion coefficient of Cu^{1+}, determined from NMR line narrowing,[63] is $D(Cu^{1+}) = 5 \times 10^{-3} \exp(-1.25\ eV/kT) \cong 2 \times 10^{-12}\ cm^2\ s^{-1}$ at 400 °C. The diffusion coefficient of In, determined with a radioactive tracer experiment at 650 °C, is $D(In) = 8.0 \times 10^{-10}\ cm^2\ s^{-1}$;[50] the thermal activation energy was not measured. At 650 °C the calculated diffusion coefficient of Cu = $7 \times 10^{-10}\ cm^2\ s^{-1}$ is essentially the same as that of In, surprisingly, given that Cu is considered to be less strongly bound in the chalcopyrite than In. Assuming the same activation energies for Cu and In diffusion, at 400 °C both diffusion coefficients, D, will be $\sim 2 \times 10^{-12}\ cm^2\ s^{-1}$. For a 24 h long diffusion time, t, the diffusion length $\sqrt{Dt}$ will be 4 μm, far longer than the ∼100 nm spacing of the Cu-poor interphases. Therefore, as far as Cu and In atomic and associated defect distributions are concerned, the crystal is equilibrated at 400 °C. While at high temperature the crystal may be homogeneous single-phase $CuInS_2$ with a high concentration of V_{Cu}, upon cooling it will segregate out V_{Cu} to interphases at temperatures down to 400 °C.

In the present case the Cu-poor interphases form along the (112) pseudotwin boundary. Free surfaces of $CuInS_2$ can also become Cu poor.[44,64] At grain boundaries, to explain the passivation to recombination of photoexcited holes in polycrystalline thin film $CuInSe_2$ solar cells, Jaffe and Zunger argue that Cu depletion at grain boundaries sets up an electric field that repels holes.[65] Similar to this Cu depletion from free surfaces, grain boundaries, and device interfaces,[10] the (112) pseudotwin boundaries of the present crystal may function as nucleation sites for the Cu-poor interphases.

With the diffusion lengths of Cu and In being much larger than the spacing between the interphase layers, one may expect some interphases to grow at the expense of others due to Ostwald ripening. This might have occurred in the present crystal because only single thickness interphases are found fully surrounded by bulk $CuInS_2$; these may be the first stage of V_{Cu} segregation. Single thickness layers that extend through the entire crystal, and even more so, double layers, may already have benefitted from Ostwald ripening. The observations by Cattarin and Guerriero suggest that ripening may continue under appropriate crystal growth conditions.[25] The peculiar structural aspect of a filamentary $CuInS_2$ bulk observed by Cattarin et al.[26] was not seen in the present crystal.

4.3. Optical Band Gap. The optical gap determined from the transmission spectrum of 1.47 eV disagrees with the accepted band gap value for $CuInS_2$ of 1.53 eV.[8,9,28,66,67] It lies close to the 1.48−1.50 eV optical gaps reported by Cattarin et al.[40] in their work with photoanodes made of $CuInS_2$ that had filamentary morphology. The optical gap of 1.47 eV must originate in the interphase layers. As these occupy ∼1% of the thickness of the 0.3 mm thick sample, the sum of their thicknesses is ∼3 μm. If the joint valence band (VB)−conduction band (CB) states in the interphase layers remain localized on the Cu atoms,[66] they will absorb light as strongly as bulk $CuInS_2$ does. Then the reduction of the Cu concentration to ∼2/3 of that in bulk $CuInS_2$ will reduce the strength of optical absorption in the interphase by only 1/3 from that of $CuInS_2$.

https://dx.doi.org/10.1021/acs.jpcc.0c08872
J. Phys. Chem. C 2020, 124, 26415−26427

Analyses and computations highlight that the valence band maxima (VBM) in chalcopyrites lie at much higher electron energy (lower ionization energy) than in the equivalent II−VI semiconductors.[8,45,46,66] The antibonding Cu d−X p hybrid states in the valence band are the cause. Reducing the copper content reduces the antibonding repulsion and hence lowers the energy of the VBM. The conduction band minimum (CBM) is similarly displaced, but usually less strongly because of the compensating Coulombic attraction between the 2 V_{Cu}^{1-} and In_{Cu}^{2+} defects. Thus, band structure calculations suggest that the band gap will increase as the Cu content is reduced.[65]

Given the absence of experimental data for $CuInS_2$ that verify these theoretical predictions, we resort to relevant observations in its $CuInSe_2$ homologue. Experiments along the Cu_2Se−In_2Se_3 quasi-binary indeed agree with theory,[68] in that reducing Cu raises the band gaps of Cu−In−Se compounds, from chalcopyrite $CuInSe_2$ (Cu:In = 1.00) at 0.99 eV, to $CuIn_3Se_5$ (Cu:In = 0.33) at 1.17 eV, to $CuIn_5Se_8$ (Cu:In = 0.20) at ∼1.23 eV. As well, the corresponding electron affinities rise from 4.26 eV to 4.48−4.62 eV. This rise in bandgap and electron affinity with Cu depletion was observed in CdS/$CuInSe_2$ solar cells.[34] Maeda et al.[68] found that within the $CuInSe_2$ homogeneity range decreasing the Cu concentration does not change the gap, while the gap of the $CuIn_3Se_5$ phase does increase gradually, again in agreement with theoretical prediction.

Returning to the sulfide, Shay, Neumann, and Wasim[8,46,66] argue that the sensitivity of the bandgap value to Cu deficiency will be proportional to the degree of d−p hybridization, which is 34% in $CuInSe_2$ and 45% in $CuInS_2$.[8] This would mean that the energy positions of the VBM and the CBM in Cu−In−S compounds will exhibit a more pronounced drop with Cu depletion than of the Cu−In−Se compounds. In computations, this trend is borne out for the band gaps for $CuInS_2$ (1.45 eV) and $CuIn_5S_8$ (1.58 eV) and in the lowering of the CBM energy (i.e., increasing electron affinity) by 0.50 eV.[37] However, the experimentally measured values for thiospinel-structure $CuIn_5S_8$ do not agree. An indirect gap was detected at 1.29−1.31 eV and a direct gap at 1.51 eV, both lower than the $CuInS_2$ gap of 1.53 eV.[42,43,69] On the other hand, increased open-circuit voltage in $CuInS_2$/CdS solar cells is attributed to reduced interface recombination, caused by an increase of the band gap by Cu depletion.[10] While this observation deserves further analysis, the directly measured optical absorption edge of the present crystal agrees with neither the theoretical prediction for a Cu-deficient Cu−In−S phase, nor can it be linked to values observed for $CuIn_5S_8$. Likewise, currently available experimental data do not enable verification of the theoretically predicted band edge offsets between $CuInS_2$ bulk and interphase layers and, further, of their possible consequences for barriers or quantum wells.[37] As an aside, our observation that the edge of interphase disks can be moved like a zipper by the electron beam of the microscope suggests that the coherent strain between bulk and interphase is small and hence may have little effect on band edge positions.

In summary, the observed value of the optical gap of 1.47 eV is ascribed to the Cu-poor interphase, in disagreement with theoretical predictions for Cu-poor bulk phases. The VBM and CBM positions of the interphase and its band edge offsets to $CuInS_2$ remain to be determined.

4.4. Electronic Transport and Photoresponse. The electron mobility of 0.1 $cm^2\ V^{-1}\ s^{-1}$ is much lower than literature values, which range from 9 to 338 $cm^2\ V^{-1}\ s^{-1}$.[6,9,22,49,55] Only in p-type $CuInS_2$, made p-type by annealing in sulfur, a similarly low hole mobility of 0.1 $cm^2\ V^{-1}\ s^{-1}$ has been reported.[57] Early on, nearly complete donor−acceptor self-compensation was speculated to cause electron localization, hence low mobility, with the residual donor defects being In_{Cu} and V_S.[55] But charge carriers are scattered only weakly at highly symmetric grain boundaries like the (112) pseudotwin boundary, and a free-carrier mobility of 0.1 $cm^2\ V^{-1}\ s^{-1}$ would imply a mean free electron path smaller than the interatomic distance. Therefore, the observed low electron mobility must be caused by trapping associated with the disk-like layers of the Cu-poor interfacial phase. An alternative interpretation, arising from the performance of lamellar $CuInS_2$ photochemical electrodes by Cattarin et al.,[25] invokes barriers to charge transport. These authors find that the $CuInS_2$ bulk is n-type while the interphase lamellae are either insulating or p-type, such that they may form n/i/n or n/p/n barriers in the conduction band. Because the interphase layers in our crystal are so thin, any barrier to electron transport may not be built up by a space charge, but instead may be caused by an offset in the CB edges and/or by interface dipoles. Unfortunately, around room temperature the experimentally determined T-dependence of the mobility, $\delta\mu_n/\delta T$, is an unreliable guide to a physical mechanism, as the transition from impurity scattering to lattice scattering can change the value and even the sign of $\delta\mu_n/\delta T$.[27,49,55]

The electrical resistivity at room temperature of $2.7 \times 10^6\ \Omega\cdot$cm is high because of the low electron mobility and the low electron concentration of $2.3 \times 10^{13}\ cm^{-3}$. High resistivities have been observed in as-grown crystals,[22,55,70] in crystals equilibrated with Zn (hence Cu-poor),[27] and in thin films prepared without excess Cu.[10,71] As nanometer thick Cu-poor interphases cannot be detected by the routine XRD analysis typically employed in thin-film solar cell work, some of the highly resistive material of earlier studies also may have been stoichiometric $CuInS_2$ with interphase inclusions. With the reservation that the thermal activation energy of the electrical resistivity includes both electron density and mobility, the value measured here of 87 meV is compatible with the donor ionization energies identified in $CuInS_2$, which range from 5 to 570 meV.[45,56−61]

The observations made on the present crystal agree with earlier work that invoked self-compensation due to the additional degree of freedom inherent in a two-cation structure of differing valency.[51,58,72−74] The widely accepted mechanism postulated by Zhang and Zunger[45] is the formation of electrically neutral $[V_{Cu}^{1-}In_{Cu}^{2+}V_{Cu}^{1-}]$ defect triplets, which this study confirms. Such self-compensation will raise the electrical resistivity. The sample's high resistivity also suggests that the atomic ratio of V_{Cu} to In_i, estimated from EDS data to be 1.34, likely lies very close to 2, as a large excess of relatively shallow In_i donors would greatly increase the concentration of free electrons.[56]

The spectral photoresponse, shown in Figure S5, extends out to 1050 nm (1.18 eV) illumination and agrees with the photoconductivity spectrum reported by Cybulski et al.[27] for n-$CuInS_2$. The corresponding deep levels most likely lie in the interphases and the partial dislocations at their perimeters.

4.5. Implications for $CuInS_2$ Thin Films. The interphase layers segregate out on (112) pseudotwin boundaries, which are planar defects with very small interfacial energies. Polycrystalline thin-film solar cells contain planar defects

https://dx.doi.org/10.1021/acs.jpcc.0c08872
J. Phys. Chem. C 2020, 124, 26415−26427

with substantially larger interfacial energies, which are more conducive to the segregation of planar second phases: free surfaces during film growth, grain boundaries, and device interfaces including heterojunctions and electrical contacts. While such planar defects will be stable locations for Cu-poor interphases, these can be detected only by high-resolution electron microscopy.[33] In the few micrometers thick films employed for solar cells, the Cu-deficient material will not be sufficiently thick to reduce the optical gap and therefore will not be visible in optical absorption. However, in solar cell work to date, many electrical effects have been imputed to native compositional inhomogeneities. To establish reference samples, these electrical effects must be correlated once with structural and compositional analysis on the nanometer scale. After that, electrical techniques will remain the methods of choice for routine evaluation of device films. Electric fields associated with grain boundaries including polarity-induced band bending may confine photogenerated minority carriers, so that columnar grains will function as minority carrier conduits.[51] By use of this argument, Cu-depleted grain boundaries have been inferred from high minority carrier lifetime. On the other hand, interphases at intragrain boundaries may reduce the electron mobility as they do in the single crystal. Copper-depleted layers are likely to form at solar cell heterojunctions. These may favor or oppose the collection of photogenerated carriers. Indeed, $CuInS_2$ heterojunction solar cells have been made more efficient by using buffer layers that are impervious to Cu in diffusion. Pursuing a comparable goal on the Cu-rich side, $CuInS_2$ films have been deposited with excess Cu and S to raise their chemical potentials above those in $CuInS_2$; the ensuing macroscopic cover of excess Cu_2S must be etched away before the heterojunction is formed.[13] Such empirical approaches have been central to the development of thin-film chalcopyrite heterojunction solar cells. Quantitative device design and simulation will require further experimental data, acquired on the nanometer scale, about the properties of $CuInS_2$ and of its interfaces with buffer and contact materials.

5. CONCLUSIONS AND OUTLOOK

While the electrical transport properties of chalcopyrite-type semiconductors are adjusted by changing stoichiometry instead of substitutional doping, setting the solar cell performance of $CuInS_2$ thin films by changing their Cu content has produced contradictory results. The present study of a single crystal shows that "Cu-poor" $CuInS_2$ is biphasic on the nanometer scale. Cu deficiency segregates out readily along (112) pseudotwin boundaries, where the deficiency organizes in the form of $[V_{Cu}^{1-}In_i^{2+}V_{Cu}^{1-}]$ defect triplets. These are electrically self-compensating and neutral. In polycrystalline thin-film solar cells Cu deficiency will similarly segregate because both Cu and In are fast diffusers at the substrate temperatures employed for solar cell fabrication. Therefore, designing $CuInS_2$ material for solar cells will need structural and compositional information at the nanometer scale, acquired after both film growth and cell fabrication, coupled with information about optical gap, band edge offsets, and electrical transport properties. The present study suggests three directions toward obtaining the needed quantitative understanding of hence better control over this solar cell material. One is an exploration of type and magnitude of electrical conductivity achievable by varying the sulfur pressure along the Cu-poor phase boundary of $CuInS_2$. A second study would trace out the Cu-rich phase boundary in the same way. The result would enable the quantitative design of the $CuInS_2$ solar cell absorber layer. Coupled with these material studies, values of the ionization energy and electron affinity of the interphases are needed to understand how they affect carrier transport properties as well as the open-circuit voltage of solar cells made with biphasic material. The electron states of the interphase of this study may be quantum confined in the ⟨112⟩ direction. Current research on $CuInS_2$ (hence, nontoxic) nanocrystals[54] and quantum dots[75] may extend to exploring their ordered-defect, Cu-deficient homologues, thereby helping to clarify band edge positions, quantized levels, and optical gaps.

■ ASSOCIATED CONTENT

Supporting Information

The Supporting Information is available free of charge at https://pubs.acs.org/doi/10.1021/acs.jpcc.0c08872.

Additional analysis and characterization of $CuInS_2$ single crystal including XPS analysis of Cu 2p, In 3d, and S 2p (Figure S1); STEM-EDS mapping of Cu, In, and S (Figure S2); EDS-measured atomic percent composition of Cu, In, and S (Table S1); STEM-EDS mapping of the single and double interphase layers in the ⟨$\overline{1}11$⟩ direction (Figure S3); STEM-HAADF image showing two interfacial phases (Figure S4); and additional photoresponse data under 780 and 1050 nm illumination (Figure S5) (PDF)

■ AUTHOR INFORMATION

Corresponding Authors

Jessica J. Frick − *Department of Chemistry, Princeton University, Princeton, New Jersey 08544, United States;* orcid.org/0000-0002-1909-3118; Email: jjfrick@stanford.edu

Sigurd Wagner − *Department of Electrical Engineering, Princeton University, Princeton, New Jersey 08544, United States*; Email: wagner@princeton.edu

Authors

Guangming Cheng − *PRISM, Princeton University, Princeton, New Jersey 08544, United States;* orcid.org/0000-0001-5852-1341

Satya Kushwaha − *Department of Chemistry, Princeton University, Princeton, New Jersey 08544, United States*

Nan Yao − *PRISM, Princeton University, Princeton, New Jersey 08544, United States*

Andrew B. Bocarsly − *Department of Chemistry, Princeton University, Princeton, New Jersey 08544, United States;* orcid.org/0000-0003-3718-0933

Robert J. Cava − *Department of Chemistry, Princeton University, Princeton, New Jersey 08544, United States*

Complete contact information is available at: https://pubs.acs.org/10.1021/acs.jpcc.0c08872

Author Contributions

J.J.F. and G.C. designed the experiments. J.J.F. collected and analyzed electronic transport data with analysis assistance from R.J.C. J.J.F. collected and analyzed photoconductivity data with analysis assistance from S.W. G.C. collected and analyzed TEM data with analysis assistance from J.J.F. and N.Y. J.J.F. wrote the manuscript with assistance from G.C., S.W., and R.J.C. All

https://dx.doi.org/10.1021/acs.jpcc.0c08872
J. Phys. Chem. C 2020, 124, 26415−26427

authors have given approval to the final version of the manuscript.

Notes

The authors declare no competing financial interest.

■ ACKNOWLEDGMENTS

This manuscript is based upon work supported by the National Science Foundation Graduate Research Fellowship via Grant 1656466 awarded to J.J.F. The crystal growth was supported by the ARO MURI on topological insulators, Grant W911NF-1210461. The authors acknowledge the use of Princeton's Imaging and Analysis Center, which is partially supported by the Princeton Center for Complex Materials, a National Science Foundation (NSF)-MRSEC program (DMR-1420541). R.J.C. acknowledges Grant DE-FG02-98ER45706, and A.B.B. acknowledges Grant DE-SC0002133 from the U.S. Department of Energy for financial support.

■ REFERENCES

(1) Goryunova, N. A. *The Chemistry of Diamond-like Semiconductors*; Anderson, J. C., Ed.; MIT Press: Cambridge, MA,1965.
(2) Pauling, L. Structure of Crystals. *Ind. Eng. Chem.* **1932**, *24*, 117.
(3) Hahn, H.; Frank, G.; Klingler, W.; Meyer, A.-D.; Störger, G. Untersuchungen über ternäre Chalkogenide. V. Über einige ternäre Chalkogenide mit Chalkopyritstruktur. *Z. Anorg. Allg. Chem.* **1953**, *271* (3−4), 153−170.
(4) Grimm, H. G.; Sommerfeld, A. Über den. Zusammenhang des Abschlusses der Elektronengruppen im Atom mit den chemischen Valenzzahlen. *Eur. Phys. J. A* **1926**, *36* (1), 36−59.
(5) Kasper, H. M. Crystal Growth and Properties of Some I-III-VI_2 Compounds. In NBS Special Publication 364; Washington DC, 1972; pp 671−679.
(6) Tell, B.; Shay, J. L.; Kasper, H. M. Room-Temperature Electrical Properties of Ten I-III-VI_2 Semiconductors. *J. Appl. Phys.* **1972**, *43* (5), 2469−2470.
(7) Abrahams, S. C.; Bernstein, J. L. Piezoelectric Nonlinear Optic $CuGaS_2$ and $CuInS_2$ Crystal Structure: Sublattice Distortion in $A^IB^{III}C_2^{VI}$ and $A^{II}B^{IV}C_2^{V}$ Type Chalcopyrites. *J. Chem. Phys.* **1973**, *59* (10), 5415−5422.
(8) Shay, J. L.; Tell, B. Energy Band Structure of I−III−VI_2 Semiconductors. *Surf. Sci.* **1973**, *37*, 748−762.
(9) Hsu, T. M.; Lee, J. S.; Hwang, H. L. Photoreflectance of Sulfur-annealed Copper Indium Disulfide. *J. Appl. Phys.* **1990**, *68* (1), 283−287.
(10) Klenk, R.; Klaer, J.; Scheer, R.; Lux-Steiner, M. Ch.; Luck, I.; Meyer, N.; Rühle, U. Solar Cells Based on $CuInS_2$—an Overview. *Thin Solid Films* **2005**, *480*−*481*, 509−514.
(11) Kazmerski, L. L.; Sanborn, G. A. $CuInS_2$ Thin-film Homojunction Solar Cells. *J. Appl. Phys.* **1977**, *48* (7), 3178−3180.
(12) Mitchell, K. W.; Eberspacher, C.; Cohen, F.; Avery, J.; Duran, G.; Bottenberg, W. Progress towards High Efficiency Thin Film CdTe Solar Cells. *Sol. Cells* **1988**, *23* (1), 49−57.
(13) Braunger, D.; Hariskos, D.; Walter, T.; Schock, H. W. An 11.4% Efficient Polycrystalline Thin Film Solar Cell Based on $CuInS_2$ with a Cd-Free Buffer Layer. *Sol. Energy Mater. Sol. Cells* **1996**, *40* (2), 97−102.
(14) AbuShama, J.; Noufi, R.; Johnston, S.; Ward, J.; Wu, X. Improved Performance in $CuInSe_2$ and Surface-Modified $CuGaSe_2$ Solar Cells; *Conf. Rec. 31st IEEE Photovoltaic Specialists Conf.* New York, 2005.
(15) Hiroi, H.; Iwata, Y.; Adachi, S.; Sugimoto, H.; Yamada, A. New World-Record Efficiency for Pure-Sulfide Cu(In,Ga)S_2 Thin-Film Solar Cell with Cd-Free Buffer Layer via KCN-Free Process. *IEEE J. Photovolt.* **2016**, *6* (3), 760−763.
(16) Nakamura, M.; Yamaguchi, K.; Kimoto, Y.; Yasaki, Y.; Kato, T.; Sugimoto, H. Cd-Free Cu(In,Ga)$(Se,S)_2$ Thin-Film Solar Cell with Record Efficiency of 23.35%. *IEEE J. Photovolt.* **2019**, *9* (6), 1863−1867.
(17) Seto, J. Y. W. The Electrical Properties of Polycrystalline Silicon Films. *J. Appl. Phys.* **1975**, *46* (12), 5247−5254.
(18) Kamins, T. *Polycrystalline Silicon for Integrated Circuits and Displays*; Springer Science & Business Media: 1998.
(19) Hwang, H. L.; Sun, C. Y.; Leu, C. Y.; Cheng, C. L.; Tu, C. C. Growth of $CuInS_2$ and its Characterization. *Rev. Phys. Appl. (Paris)* **1978**, *13* (12), 745−751.
(20) Sun, C.; Hwang, H.; Leu, C.; Liu, L.; Tseng, B. Vapor Growth of $CuInS_2$ Single Crystals and its Thermodynamic Considerations. *Jpn. J. Appl. Phys.* **1980**, *19* (S3), 81.
(21) Hsu, H. J.; Yang, M. H.; Tang, R. S.; Hsu, T. M.; Hwang, H. L. A Novel Method to Grow Large $CuInS_2$ Single Crystals. *J. Cryst. Growth* **1984**, *70* (1), 427−432.
(22) Hsu, H. J.; Sun, C. Y.; Hwang, H. L. Growth of $CuInS_2$ Single Crystals by THM. *Electron. Lett.* **1984**, *20* (9), 376.
(23) Fearheiley, M. L.; Dietz, N.; Lewerenz, H. J. Phase Relations in the Cu-In-S System and Growth of Large $CuInS_2$ Single Crystals. *J. Electrochem. Soc.* **1992**, *139* (2), 512−517.
(24) Dietz, N.; Fearheiley, M. L.; Schroetter, S.; Lewerenz, H. J. Structural and Defect Characterization of $CuInS_2$ Single Crystals Grown under Elevated Pressures. *Mater. Sci. Eng., B* **1992**, *14* (1), 101−109.
(25) Cattarin, S.; Guerriero, P.; Razzini, G.; Lewerenz, H.-J. $CuInS_2$ with Lamellar Morphology: II. Photoelectrochemical Behavior of Heterogeneous Material. *J. Electrochem. Soc.* **1994**, *141* (5), 1100−1104.
(26) Cattarin, S.; Pagura, C.; Armelao, L.; Bertoncello, R.; Dietz, N. Surface Characterization of $CuInS_2$ with Lamellar Morphology. *J. Electrochem. Soc.* **1995**, *142* (8), 2818−2023.
(27) Cybulski, D.; Opanowicz, A. Electrical and Photoelectrical Properties of *n*-$CuInS_2$ Single Crystals. *Cryst. Res. Technol.* **1997**, *32* (6), 813−820.
(28) Ivanov, V. A.; Viktorov, I. A.; Gremenok, V. F. Radiative and Photoelectric Properties of $CuInS_2$ Single Crystals. *Technol. Phys.* **2002**, *47* (9), 1197−1198.
(29) Shay, J. L.; Wernick, J. H. *Ternary Chalcopyrite Semiconductors: Growth, Electronic Properties, and Applications*; Elsevier: 1975.
(30) Scheer, R.; Walter, T.; Schock, H. W.; Fearheiley, M. L.; Lewerenz, H. J. $CuInS_2$ Based Thin Film Solar Cell with 10.2% Efficiency. *Appl. Phys. Lett.* **1993**, *63* (24), 3294−3296.
(31) Mickelsen, R. A.; Chen, W. S. Development of a 9.4% Efficient Thin-Film $CuInSe_2$/CdS Solar Cell; *Conf. Rec. 15th IEEE Photovoltaic Specialists Conf.* New York, 1981.
(32) Lomuscio, A.; Rödel, T.; Schwarz, T.; Gault, B.; Melchiorre, M.; Raabe, D.; Siebentritt, S. Quasi-Fermi-Level Splitting of Cu-Poor and Cu-Rich $CuInS_2$ Absorber Layers. *Phys. Rev. Appl.* **2019**, *11* (5), No. 054052.
(33) Abou-Ras, D.; Kostorz, G.; Hariskos, D.; Menner, R.; Powalla, M.; Schorr, S.; Tiwari, A. N. Structural and Chemical Analyses of Sputtered In_xS_y Buffer Layers in Cu(In,Ga)Se_2 Thin-Film Solar Cells. *Thin Solid Films* **2009**, *517* (8), 2792−2798.
(34) Schmid, D.; Ruckh, M.; Grunwald, F.; Schock, H. W. Chalcopyrite/Defect Chalcopyrite Heterojunctions on the Basis of $CuInSe_2$. *J. Appl. Phys.* **1993**, *73* (6), 2902−2909.
(35) Bär, M.; Klaer, J.; Weinhardt, L.; Wilks, R. G.; Krause, S.; Blum, M.; Yang, W.; Heske, C.; Schock, H.-W. $Cu_{2-x}S$ Surface Phases and Their Impact on the Electronic Structure of $CuInS_2$ Thin Films − A Hidden Parameter in Solar Cell Optimization. *Adv. Energy Mater.* **2013**, *3* (6), 777−781.
(36) Bär, M.; Barreau, N.; Couzinié-Devy, F.; Weinhardt, L.; Wilks, R. G.; Kessler, J.; Heske, C. Impact of Annealing-Induced Intermixing on the Electronic Level Alignment at the In_2S_3/Cu(In,Ga)Se_2 Thin-Film Solar Cell Interface. *ACS Appl. Mater. Interfaces* **2016**, *8* (3), 2120−2124.
(37) Ghorbani, E.; Erhart, P.; Albe, K. Energy Level Alignment of Cu(In, Ga) (S, $Se)_2$ Absorber Compounds with In_2S_3, $NaIn_5S_8$, and

https://dx.doi.org/10.1021/acs.jpcc.0c08872
J. Phys. Chem. C 2020, 124, 26415−26427

$CuIn_5S_8$ Cd-Free Buffer Materials. *Phys. Rev. Materials* **2019**, *3* (7), No. 075401.
(38) Binsma, J. J. M.; Giling, L. J.; Bloem, J. Phase Relations in the System Cu_2S-In_2S_3. *J. Cryst. Growth* **1980**, *50* (2), 429−436.
(39) Verheijen, A. W.; Giling, L. J.; Bloem, J. The Region of Existence of $CuInS_2$. *Mater. Res. Bull.* **1979**, *14* (2), 237−240.
(40) Cattarin, S.; Dietz, N.; Lewerenz, H. J. $CuInS_2$ with Lamellar Morphology: I. Efficient Photoanodes in Acidic Polyiodide Medium. *J. Electrochem. Soc.* **1994**, *141* (5), 1095−1099.
(41) Thomere, A.; Guillot-Deudon, C.; Caldes, M. T.; Bodeux, R.; Barreau, N.; Jobic, S.; Lafond, A. Chemical Crystallographic Investigation on Cu_2S-In_2S_3-Ga_2S_3 Ternary System. *Thin Solid Films* **2018**, *665*, 46−50.
(42) Orlova, N. S.; Bodnar, I. V.; Kudritskaya, E. A. Crystal Growth and Properties of the $CuIn_5S_8$ and $AgIn_5S_8$ Compounds. *Cryst. Res. Technol.* **1998**, *33* (1), 37−42.
(43) Qasrawi, A. F.; Gasanly, N. M. Photoelectronic and Electrical Properties of $CuIn_5S_8$ Single Crystals. *Cryst. Res. Technol.* **2003**, *38* (12), 1063−1070.
(44) Österreicher, I.. Oberflächenspektroskopische Charakterisierung von CuInS2- Dünnschichten, PhD thesis, Justus-Liebig Universität, Giessen, Germany, 2003.
(45) Zhang, S. B.; Wei, S.-H.; Zunger, A.; Katayama-Yoshida, H. Defect Physics of the $CuInSe_2$ Chalcopyrite Semiconductor. *Phys. Rev. B: Condens. Matter Mater. Phys.* **1998**, *57* (16), 9642−9656.
(46) Wasim, S. M.; Rincón, C.; Marín, G.; Delgado, J. M. On the Band Gap Anomaly in I−III−VI_2, I−III_3−VI_5, and I−III_5−VI_8 Families of Cu Ternaries. *Appl. Phys. Lett.* **2000**, *77* (1), 94−96.
(47) Frick, J. J.; Kushwaha, S. K.; Cava, R. J.; Bocarsly, A. B. Characterization of Primary Carrier Transport Properties of the Light-Harvesting Chalcopyrite Semiconductors $CuIn(S_{1-x}Se_x)_2$. *J. Phys. Chem. C* **2017**, *121* (32), 17046−17052.
(48) Smyth, D. M. Thermodynamic Characterization of Ternary Compounds. I. The Case of Negligible Defect Association. *J. Solid State Chem.* **1976**, *16* (1), 73−81.
(49) Binsma, J. J. M.; Van Enckevort, W. J. P.; Staarink, G. W. M. CVT Growth of $CuInS_2$ and $CuGaS_2$ Assisted by VLS Mechanisms. *J. Cryst. Growth* **1983**, *61* (1), 138−156.
(50) Wißmann, S.; Becker, K. D. Tracer Diffusion of Indium in $CuInS_2$. *Solid State Ionics* **1997**, *101*−*103*, 539−545.
(51) Persson, C.; Zunger, A. Compositionally Induced Valence-Band Offset at the Grain Boundary of Polycrystalline Chalcopyrites Creates a Hole Barrier. *Appl. Phys. Lett.* **2005**, *87* (21), 211904.
(52) Abou-Ras, D.; Schorr, S.; Schock, H. W. Grain-Size Distributions and Grain Boundaries of Chalcopyrite-Type Thin Films. *J. Appl. Crystallogr.* **2007**, *40* (5), 841−848.
(53) Rose, A. *Concepts in Photoconductivity and Allied Problems*; Interscience Publishers: New York, 1963.
(54) Houck, D. W.; Assaf, E. I.; Shin, H.; Greene, R. M.; Pernik, D. R.; Korgel, B. A. Pervasive Cation Vacancies and Antisite Defects in Copper Indium Diselenide ($CuInSe_2$) Nanocrystals. *J. Phys. Chem. C* **2019**, *123* (14), 9544−9551.
(55) Look, D. C.; Manthuruthil, J. C. Electron and Hole Conductivity in $CuInS_2$. *J. Phys. Chem. Solids* **1976**, *37* (2), 173−180.
(56) Ueng, H. Y.; Hwang, H. L. The Defect Structure of $CuInS_2$. Part I: Intrinsic Defects. *J. Phys. Chem. Solids* **1989**, *50* (12), 1297−1305.
(57) Ueng, H. Y.; Hwang, H. L. The Defect Structure of $CuInS_2$. Part II: Thermal Annealing Defects. *J. Phys. Chem. Solids* **1990**, *51* (1), 1−10.
(58) Lany, S.; Zunger, A. Anion Vacancies as a Source of Persistent Photoconductivity in II-VI and Chalcopyrite Semiconductors. *Phys. Rev. B: Condens. Matter Mater. Phys.* **2005**, DOI: 10.1103/PhysRevB.72.035215.
(59) Rincón, C.; Márquez, R. Defect Physics of the $CuInSe_2$ Chalcopyrite Semiconductor. *J. Phys. Chem. Solids* **1999**, *60* (11), 1865−1873.
(60) Chen, H.; Wang, C.-Y.; Wang, J.-T.; Hu, X.-P.; Zhou, S.-X. First-Principles Study of Point Defects in Solar Cell Semiconductor $CuInS_2$. *J. Appl. Phys.* **2012**, *112* (8), No. 084513.
(61) Cao, Q.; Gunawan, O.; Copel, M.; Reuter, K. B.; Chey, S. J.; Deline, V. R.; Mitzi, D. B. Defects in Cu(In,Ga)Se_2 Chalcopyrite Semiconductors: A Comparative Study of Material Properties, Defect States, and Photovoltaic Performance. *Adv. Energy Mater.* **2011**, *1* (5), 845−853.
(62) Reynolds, S.; Brinza, M.; Benkhedir, M. L.; Adriaenssens, G. J. Photoconductivity in Materials Research. In *Springer Handbook of Electronic and Photonic Materials*; Kasap, S., Capper, P., Eds.; Springer International Publishing: Cham, 2017.
(63) Becker, K. D.; Wagner, S. Temperature-Dependent Nuclear Magnetic Resonance in $CuInX_2$ (X = S, Se, Te) Chalcopyrite-Structure Compounds. *Phys. Rev. B: Condens. Matter Mater. Phys.* **1983**, *27* (9), 5240−5249.
(64) Scheer, R.; Lewerenz, H.-J. Formation of Secondary Phases in Evaporated $CuInS_2$ Thin Films: A Surface Analytical Study. *J. Vac. Sci. Technol., A* **1995**, *13* (4), 1924−1929.
(65) Jaffe, J. E.; Zunger, A. Electronic Structure of the Ternary Chalcopyrite Semiconductors $CuAlS_2$, $CuGaS_2$, $CuInS_2$, $CuAlSe_2$, $CuGaSe_2$, and $CuInSe_2$. *Phys. Rev. B: Condens. Matter Mater. Phys.* **1983**, *28* (10), 5822−5847.
(66) Neumann, H.; Hörig, W.; Savelev, V.; Lagzdonis, J.; Schumann, B.; Kühn, G. The Optical Properties of $CuInS_2$ Thin Films. *Thin Solid Films* **1981**, *79* (2), 167−171.
(67) Mobarak, M.; Shaban, H. T.; Elhady, A. F. Electrical and Thermoelectric Properties of $CuInS_2$ Single Crystals. *Mater. Chem. Phys.* **2008**, *109* (2), 287−290.
(68) Maeda, T.; Gong, W.; Wada, T. Crystallographic and Optical Properties and Band Structures of $CuInSe_2$, $CuIn_3Se_5$, and $CuIn_5Se_8$ Phases in Cu-Poor Cu_2Se−In_2Se_3 Pseudo-Binary System. *Jpn. J. Appl. Phys.* **2016**, *55* (4S), 04ES15, 1−10.
(69) Usujima, A.; Takeuchi, S.; Endo, S.; Irie, T. Optical and Electrical Properties of $CuIn_5S_8$ and $AgIn_5S_8$ Single Crystals. *Jpn. J. Appl. Phys.* **1981**, *20* (7), L505.
(70) Bridenbaugh, P. M.; Migliorato, P. Junction Electroluminescence in $CuInS_2$. *Appl. Phys. Lett.* **1975**, *26* (8), 459−460.
(71) Herberholz, R.; Nadenau, V.; Rühle, U.; Köble, C.; Schock, H. W.; Dimmler, B. Prospects of Wide-Gap Chalcopyrites for Thin Film Photovoltaic Modules. *Sol. Energy Mater. Sol. Cells* **1997**, *49* (1), 227−237.
(72) Lany, S.; Zunger, A. Intrinsic D-X Centers in Ternary Chalcopyrite Semiconductors. *Phys. Rev. Lett.* **2008**, *100* (1), No. 016401.
(73) Zhao, Y.-J.; Persson, C.; Lany, S.; Zunger, A. Why Can $CuInSe_2$ Be Readily Equilibrium-Doped *n*-Type but the Wider-Gap $CuGaSe_2$ Cannot? *Appl. Phys. Lett.* **2004**, *85* (24), 5860−5862.
(74) Migliorato, P.; Shay, J. L.; Kasper, H. M.; Wagner, S. Analysis of the Electrical and Luminescent Properties of $CuInSe_2$. *J. Appl. Phys.* **1975**, *46* (4), 1777−1782.
(75) Fuhr, A.; Yun, H. J.; Crooker, S. A.; Klimov, V. I. Spectroscopic and Magneto-Optical Signatures of Cu^{1+} and Cu^{2+} Defects in Copper Indium Sulfide Quantum Dots. *ACS Nano* **2020**, *14* (2), 2212−2223.